Results in Physics 75 (2025) 108340

Contents lists available at ScienceDirect

Results in Physics

journal homepage: www.elsevier.com/locate/rinp

Characterization of charge state distributions in Near-Infrared Laser-Driven tin plasmas for efficient EUV generation

Jang Hyeob Sohn [a], Hyun-Kyung Chung [b], Hyungyu Yu [a], Inki Jeong [c], Sang June Hahn [c], Young-Gui Yoon [c], Hyyong Suk [a], Byoung Ick Cho [a,d,*]

[a] Department of Physics and Photon Science, Gwangju Institute of Science and Technology (GIST), Gwangju 61005, South Korea
[b] Korea Institute of Fusion Energy (KFE), Daejeon 34133, South Korea
[c] Department of Physics, Chung-Ang University, Seoul 06974, South Korea
[d] Center for Relativistic Laser Science, Institute for Basic Science (IBS), Gwangju 61005, South Korea

ARTICLE INFO

Keywords:
EUV light source
Laser-produced plasma
Charge state distribution

ABSTRACT

In this paper, the charge state distributions of extreme ultraviolet (EUV) light source plasmas produced by near-infrared-wavelength lasers are systematically characterized. The spatiotemporal properties of laser-irradiated planar tin targets are examined using radiation-hydrodynamic simulations and non-local thermodynamic equilibrium calculations. Focusing on the distributions of Sn^{11+}–Sn^{14+} ions, which are primarily responsible for "in-band" EUV emissions, a mean charge state of 12.5 is identified as the optimal ionization level for efficient EUV generation. This prediction is consistent with the experimental observation by Behnke *et al.* (2021) of short-wavelength spectra in the 7–10 nm range, where the contributions of the Sn^{11+}–Sn^{14+} ions are well identified. Simulations further reveal that spatially and temporally uniform pulses more efficiently achieve the optimal mean charge state, producing up to 45 % more Sn^{11+}–Sn^{14+} ions than Gaussian pulses of the same energy. These findings provide foundational insights for advancing laser-driven EUV light sources for industrial applications.

Introduction

Developing efficient extreme ultraviolet (EUV) light sources is critical for advancing nanolithography technologies. Currently, EUV light is primarily generated using tin laser-produced plasmas (tin-LPPs) [1–6]. Highly ionized tin-LPPs emit the *in-band* radiation within the 13.5 nm ± 1 % range, where Mo/Si multilayer mirrors exhibit peak reflectivity [7,8]. CO_2-gas lasers operating at a wavelength of 10.6 μm are the standard drivers for tin-LPPs owing to their high conversion efficiency (CE) of laser energy into the in-band radiation [3,4]. However, their low wall-plug efficiency in converting electrical energy to laser light has spurred interest in more efficient solid-state lasers at near- and mid-infrared wavelengths, which offer additional advantages, such as compactness and flexible pulse shaping [9–11].

Building on the widespread utilization of 1.064-μm Nd:YAG lasers and the significant progress in the development of 1.88-μm Tm:YLF lasers [9,12–14], recent studies on 1- and 2-μm laser-driven tin plasmas have confirmed their potential as EUV light sources [15–24]. Notably, the 2-μm laser-driven sources have demonstrated nearly double the CE of Nd:YAG lasers, primarily owing to the substantially reduced reabsorption losses [17–19]. Despite these advances, near-infrared lasers have rarely achieved CEs comparable to CO_2 lasers, underscoring the need for more comprehensive and systematic modeling to identify the optimal conditions for maximizing efficiency.

In tin-LPPs, the in-band emissions are predominantly produced by highly charged Sn^{11+}–Sn^{14+} ions [25–28]. Therefore, understanding and controlling their charge state distributions is crucial for enhancing EUV emissions around 13.5 nm. Although many studies have attempted to optimize CE by varying laser parameters such as intensity [16–22,29–35], pulse shape [11,22], duration [15–17,20,36,37], and focal spot [38–40], most efforts remain somewhat phenomenological. Particularly, the optimal laser intensity is often described in terms of achieving a suitable temperature or ionization level without a quantitative characterization of the charge state distributions as a function of specific laser parameters. This gap has led to inconsistencies in the reported optimal parameters across experiments, indicating the necessity of a quantitative understanding of the Sn^{11+}–Sn^{14+} populations as a basis for optimizing tin-LPPs.

* Corresponding author.
E-mail address: bicho@gist.ac.kr (B.I. Cho).

https://doi.org/10.1016/j.rinp.2025.108340
Received 7 April 2025; Received in revised form 11 June 2025; Accepted 21 June 2025
Available online 22 June 2025

From a diagnostic perspective, the spectral complexity near 13.5 nm, due to numerous closely spaced transition lines, makes it challenging to directly determine ion populations [27,28,41,42]. Instead, Torretti *et al.* demonstrated that examining emission lines in the 7–10 nm range, where Sn^{11+}–Sn^{14+} ions have more distinct and identifiable features, provides a promising approach for experimentally assessing their populations [25,26].

In this study, the charge state distributions in tin plasmas produced by 2-μm lasers are systematically investigated using radiation-hydrodynamics (RHD) simulation coupled with non-local thermodynamic equilibrium (NLTE) population kinetics codes. By examining the spatiotemporal evolution of Sn^{11+}–Sn^{14+} ion distributions over a range of laser intensities, we identify a suitable ionization condition for efficient EUV generation. The results are also compared with those of 1-μm laser plasmas. Calculations of emission lines in the 7–10 nm range are used for experimental validation and presented as a diagnostic tool for Sn^{11+}–Sn^{14+} populations. Furthermore, we explore how spatial and temporal pulse shaping can enhance EUV generation, providing insights into advanced plasma control strategies.

Method

The evolution of tin-LPPs was simulated using FLASH, a finite-volume Eulerian code with adaptive mesh refinement that incorporates thermal conduction, multigroup radiation transport, and laser energy deposition with ray tracing [43]. In the simulations, planar solid tin targets were irradiated by a normally incident laser in a two-dimensional axisymmetric geometry, with the Z-axis as the axis of symmetry. The laser pulse had a Gaussian spatial profile with a 100-μm full width at half-maximum (FWHM) and a non-Gaussian temporal profile with a 5-ns FWHM, typical Q-switched laser pulses (see Fig. 2 (b)). Plasma properties obtained from the two-dimensional simulation domain were postprocessed by rotating them around the Z-axis to reconstruct a three-dimensional plasma structure.

Equation-of-state tables for tin were generated using the Frankfurt equation-of-state (FEOS) code, which models a wide range of material states, ranging from low-temperature liquid–gas mixtures to high-temperature plasmas [44]. The group-averaged opacities of tin were calculated using the collisional-radiative (CR) population kinetics model FLYCHK [45]. According to Griem's criterion, local thermodynamic equilibrium (LTE) conditions for 13.5-nm radiation are valid only at electron densities that exceed 10^{20} cm^{-3} several times for near-infrared laser wavelengths [46]. As most of the in-band emissions occur at densities far below the critical electron density (N_c [cm^{-3}] $= 1.1 \times 10^{21}/\lambda_{\mu m}^2$, where $\lambda_{\mu m}$ is the laser wavelength), NLTE calculations are indispensable for accurately describing tin-LPPs. FLYCHK is widely applicable to various elements and plasma conditions [47–49], and its predictive capability for ionization distributions has been validated through numerous experimental comparisons [50–53].

To accurately calculate short-wavelength spectra involving a large number of electric dipole (E1) $\Delta n \geq 1$ transitions—such as $4p^6 4d^m$–$(4p^5 4d^m 5s,\ 4p^5 4d^m 5d,\ 4p^5 4d^m 6s,\ 4p^5 4d^m 6d)$ [25]—we employed STAPEC, an improved spectral calculation module of FLYCHK. FLYCHK employs a screened hydrogenic formalism based on principal quantum numbers and, in principle, can describe such transitions. However, its simplified atomic data limits the accuracy of spectral predictions when compared to experimental results. To address this limitation, STAPEC incorporates configuration-averaged states and represents transition lines using the unresolved transition array formalism [54]. The spectral calculation proceeds as follows. First, FLYCHK performs a CR calculation to determine the population of each configuration without resolving the angular momentum sublevels. Then, STAPEC redistributes these populations among the different l states within each configuration based on a Boltzmann distribution. Finally, the emission spectrum is constructed by considering the transition probabilities and line-broadening effects for all possible transitions between the relevant states. For each short-wavelength spectrum, this approach typically involves up to one million $\Delta n \geq 1$ transitions, leading to spectral predictions that show good agreement with experimental observations.

Because tin-LPPs are nonuniform and cannot be represented by a single temperature-density pair, multiple plasma conditions must be considered simultaneously. In this study, we employed a multizone radiation transport model to systematically analyze plasmas generated by laser pulses with nonuniform spatial intensity profiles [18,55,56]. The three-dimensional plasma was treated as a collection of multiple homogeneous zones, as illustrated in Fig. 1. Using the temperature and density distributions from the RHD simulations, the charge state distribution, emissivity, and opacity of each zone were determined from NLTE calculations for a common temperature–density grid ranging 5–100 eV in temperature, and 10^{-6}–10^{-2} g/cm^3 in mass density. Each plasma zone was assumed to be a 100-nm-thick homogeneous slab to allow FLYCHK to incorporate self-absorption effects. The emissivity was calculated considering all radiative bound–bound, bound–free, and free–free transitions, whereas the opacity also included electron scattering contributions [49]. The overall emission spectra were obtained by integrating the spectral contributions from all the radiative zones along the line of sight toward a virtual detector at a 60° angle to the laser axis. The model also accounts for the reabsorption and distortion of inner zone emission spectra by the opacities of surrounding outer zones, thereby ensuring accurate spectral predictions. It is noted that the plasma is indeed anisotropic, particularly in the low-charge-state regions surrounding the hot EUV-emitting core. However, the reabsorption of Sn^{11+}–Sn^{14+} emission lines in the 7–10 nm window by the surrounding plasma is minimal. As a result, the spectral features are largely unaffected by the viewing angle. The choice of detection angle may be a practical consideration in experimental setups. In this work, since a 60° detection angle has been commonly adopted in earlier studies [15–19,22], we chose the same configuration to ensure consistency and comparability with previous work.

Results

Plasma characterization at various laser intensities

Time-dependent space-averaged charge state distributions for a tin plasma driven by a 2-μm laser at 4×10^{10} W/cm^2 are shown in Fig. 2(a). As laser power increases, the plasma undergoes rapid ionization and exhibits temporally varying charge state distributions. By $t = 3$ ns, highly charged Sn^{11+}–Sn^{14+} ions begin to form. Near the laser peak ($t =$ 4–5 ns), their abundance reaches its maximum, and the plasma attains

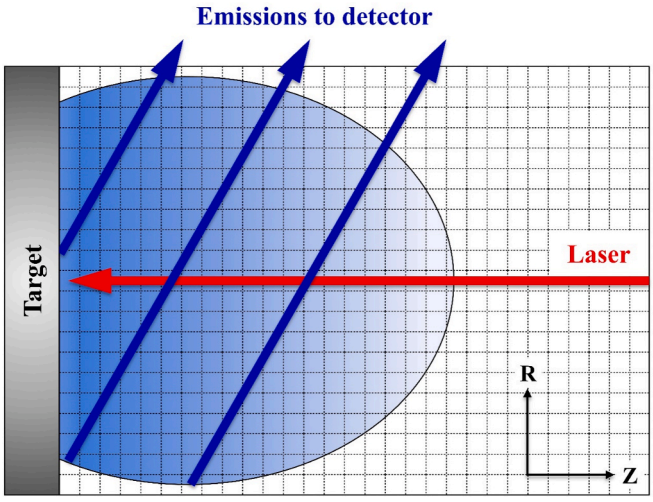

Fig. 1. Simulation setup using the multizone radiation transport model.

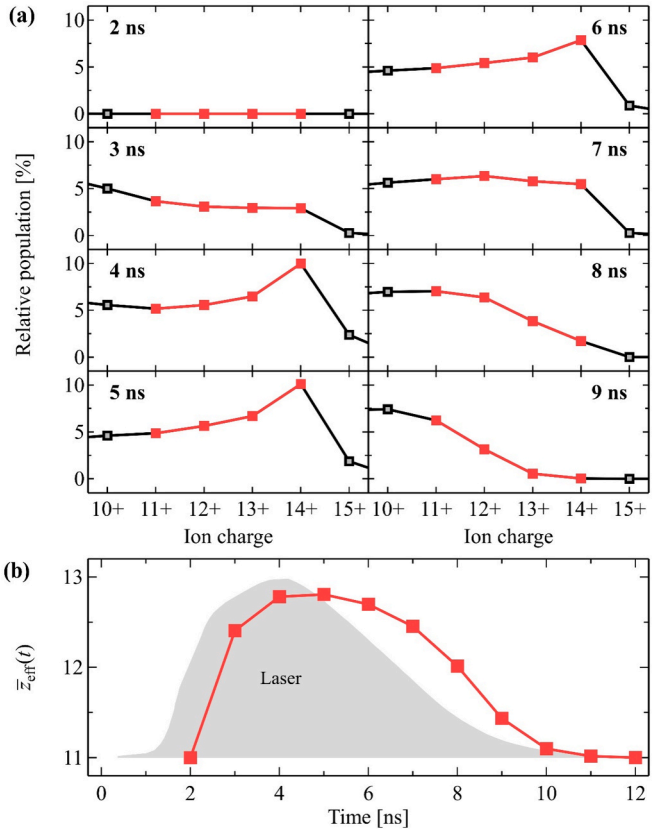

Fig. 2. (a) Time-dependent space-averaged charge state distributions of a tin plasma driven by a 2-μm-wavelength laser at a peak intensity of 4×10^{10} W/cm^2. Sn^{11+}–Sn^{14+} are highlighted in red. (b) Corresponding temporal evolution of the effective mean charge, representing the average charge state of Sn^{11+}–Sn^{14+} ions. The temporal profile of the laser pulse is shown for reference.

its highest ionization level. As the plasma cools, the charge state distribution gradually shifts toward lower ionization levels.

The effective mean charge, $\bar{z}_{eff}(t)$, which represents the average charge state of Sn^{11+}–Sn^{14+} ions, is shown in Fig. 2(b). It reaches a maximum of ~ 12.8 between $t = 4$ and 5 ns and then gradually declines. This temporal evolution closely follows the laser profile, indicating the critical role of laser pulse shaping in optimizing the ionization dynamics.

The spatial distributions of the electron temperatures, densities, and mean charge states at the laser peak are shown in Fig. 3 for different laser intensities. The temperature peaks near the target surface (30–40 μm from the surface) and decreases gradually with distance, whereas the density drops logarithmically, localizing the highly charged ions close to the target surface. The 50 % and 99 % contours of Sn^{11+}–Sn^{14+} ions delineate the regions generating most of the in-band emissions, which span a range of temperatures and charge states. At low intensities (Fig. 3 (d)), Sn^{11+}–Sn^{14+} ions are scarce; however, increasing the intensity expands both the overall ionization level and the regions dominated by these charge states. At very high intensities (Fig. 3(f)), over-ionization leads to a "hole" in the 99 % contour, reducing EUV generation efficiency.

To quantify the ionization level that leads to the efficient production of Sn^{11+}–Sn^{14+} ions, the space–time-averaged effective mean charge $\bar{Z}_{eff}$ is defined as follows:

$$\bar{Z}_{eff} = \frac{\int \sum_{z=11}^{14} z n_z(t) dt}{\int \sum_{z=11}^{14} n_z(t) dt} = \frac{\int \bar{z}_{eff}(t) n_{eff}(t) dt}{\int n_{eff}(t) dt}. \quad (1)$$

Here, z is the charge state; $n_z(t)$ is the population of ions in the charge state z at time t; and $n_{eff}(t)$ is the total population of Sn^{11+}–Sn^{14+} ions. This metric characterizes the representative charge state in regions that are primarily responsible for the in-band emissions.

A series of simulations were performed to investigate how the Sn^{11+}–Sn^{14+} populations and $\bar{Z}_{eff}$ vary with laser intensity in the range of 0.6–15 × 10^{10} W/cm^2. Fig. 4 shows the normalized ratio N_{eff}/E—the total number of Sn^{11+}–Sn^{14+} ions integrated over space and time per unit pulse energy—and the corresponding $\bar{Z}_{eff}$, plotted as a function of the 2-μm laser intensity. As the intensity increases, N_{eff}/E initially increases, peaks at 4×10^{10} W/cm^2, and then decreases. Below this

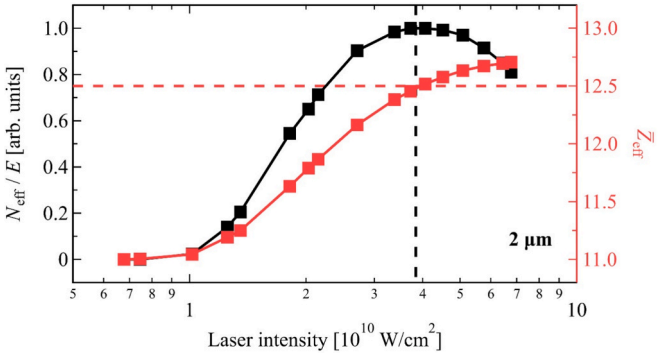

Fig. 4. (left axis) Normalized ratio N_{eff}/E, where N_{eff} is the total number of Sn^{11+}–Sn^{14+} ions and E is the pulse energy, plotted as a function of the 2-μm laser intensity. (right axis) Corresponding space–time-averaged effective mean charge $\bar{Z}_{eff}$. The vertical and horizontal dashed lines indicate the optimal laser intensity and effective mean charge, respectively, for efficient generation of Sn^{11+}–Sn^{14+} ions.

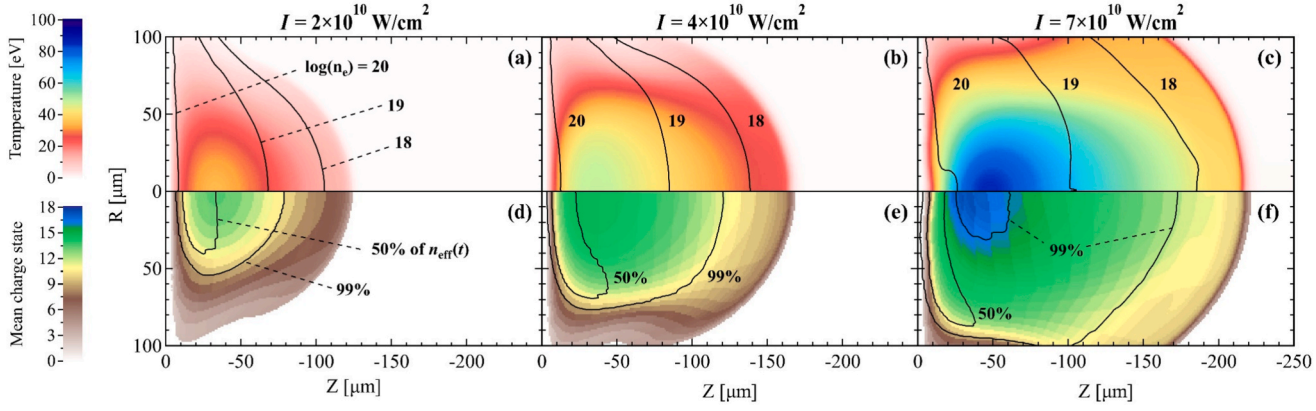

Fig. 3. (a)–(c) Spatial distribution of electron temperatures and densities at $t = 4$ ns. (d)–(f) Mean charge states and regions containing 50 % and 99 % of Sn^{11+}–Sn^{14+} ions of tin plasmas produced by the 2-μm laser at various peak intensities.

optimum intensity, insufficient ionization limits the formation of Sn^{11+}–Sn^{14+} ions, whereas above this intensity, overionization impedes the efficient laser-to-EUV conversion. Concurrently, $\overline{Z}_{eff}$ increases from a lower limit of 11 and reaches ~ 12.5 at the optimal intensity.

Fig. 5 presents analogous results for the 1-μm laser. In this case, N_{eff}/E peaks at a higher intensity of 7 × 10^{10} W/cm^2, and this maximum value is about 90 % of that for the 2-μm laser. Although the $\overline{Z}_{eff}$ curve follows a similar pattern, the intensity required by the 1-μm laser to achieve a comparable $\overline{Z}_{eff}$ is approximately 1.9 times higher than that of the 2-μm laser. This intensity scaling difference aligns with the previously reported values (1.9–2.4) [17–19], validating our plasma characterization methodology. Together, these findings demonstrate that a 2-μm laser achieves optimal conditions at significantly lower intensities than a 1-μm laser.

Assuming that the in-band EUV radiation is approximately proportional to the number of Sn^{11+}–Sn^{14+} ions, with comparable spectral contributions from each charge state, the intensity-dependent analysis of N_{eff}/E and $\overline{Z}_{eff}$ suggests that $\overline{Z}_{eff} \approx 12.5$ corresponds to the highest efficiency in generating the in-band radiation for both laser wavelengths. This value is consistent with the reported average charge state of the Nd:YAG laser-driven tin plasma at the optimal 13.5-nm radiation conditions [27]. Notably, this approach provides insights into the optimal CE conditions without requiring detailed modeling of 13.5-nm atomic transitions. Even NLTE codes with simplified atomic data, such as FLYCHK, can offer valuable guidance for predicting EUV yield by analyzing tin-LPP ionization distributions.

Experimental monitoring of charge state distribution

The charge state distributions of highly ionized tin plasmas can be determined from experimental data through spectral analysis in the short-wavelength region of 7–10 nm. Emission spectra corresponding to various charge state distributions at different laser intensities are calculated for the 2-μm laser, as shown in Fig. 6. These spectra and charge state distributions are time-integrated over 15 ns by summing instantaneous results in 1-ns steps. The spectral shapes exhibit significant sensitivity to charge state distributions. As the plasma becomes more ionized with increasing laser intensity, the emission features from higher charge states become more prominent at shorter wavelengths. The relative intensity of each emission provides an intuitive representation of charge state distributions. Consequently, the charge state distributions of the highly ionized plasma in the experiments can be inferred by comparing the short-wavelength spectra with those obtained from the simulations.

Although detailed modeling of the 13.5-nm radiation spectrum and CE is beyond the scope of this work due to the use of simplified atomic data, comparison with existing experimental results provides useful insights. Behnke *et al.* [18] reported experimentally measured CE as a function of laser intensity. For a 2-μm laser, a maximum CE of approximately 3 % was observed at an intensity of around 1 × 10^{11} W/cm^2. Although this value differs from the predicted optimal intensity (as shown in Fig. 4), the measured emission spectrum in the 7–10 nm range closely resembles the calculated spectrum at the optimal $\overline{Z}_{eff}$, as illustrated in Fig. 6. This strong similarity suggests that the $\overline{Z}_{eff}$ under Behnke *et al.*'s optimal condition is close to our predicted value of 12.5. This comparison supports the robustness of our approach in capturing the charge state distribution relevant to the in-band emission and offers valuable insight into the plasma conditions that optimize CE.

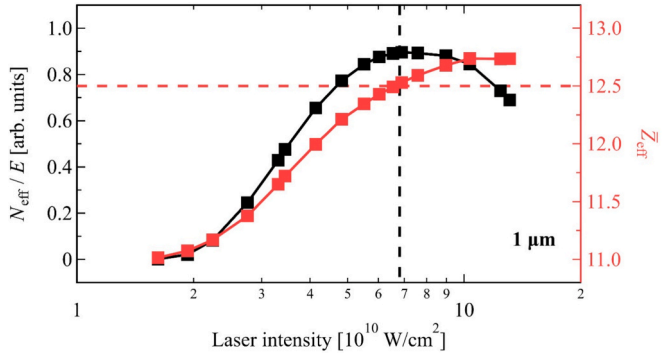

Fig. 5. Same as Fig. 4 but for 1-μm laser. N_{eff}/E is normalized based on the values in Fig. 4.

Pulse shaping for enhanced EUV light source

Figs. 7–9 present simulations in which 2- and 1-μm laser pulses with spatially Gaussian and temporally non-Gaussian profiles (hereafter, Gaussian pulses) are reshaped into spatially flat-top and temporally box-shaped pulses (flat-top pulses) with the same pulse energy and beam area. The reshaped pulses have a beam width of 120 μm and a duration of 9.5 ns, resulting in approximately 46 % lower peak intensities than those of the Gaussian pulses.

The Gaussian pulses create regions of over- and underheating; that is, high-intensity central regions raise temperatures to approximately 50 eV, whereas lower-intensity wings underheat the plasmas, leading to inefficient laser energy usage (see Fig. 7). In contrast, flat-top pulses can mitigate these heating imbalances by adopting a uniform profile, allowing the optimal mean charge state to be reached with significantly less laser energy. This improved energy distribution enables the pulse duration to be extended while maintaining the same total pulse energy. Consequently, the flat-top pulses further stabilize $\overline{z}_{eff}(t)$, keeping it near the optimal value over a prolonged period (Fig. 8). This configuration enables a more uniform ionization process, increasing N_{eff} by 45 % for both 2- and 1-μm lasers compared to Gaussian pulses at $\overline{Z}_{eff} = 12.5$ (Fig. 9). Although an increase in N_{eff} does not directly quantify CE gains, it strongly suggests an improvement in CE. These findings are consistent with the previous reports that spatiotemporally uniform pulses yield higher CEs than Gaussian pulses [11,19,22].

Conclusion

We characterized the charge state distributions of tin plasmas produced using near-infrared-wavelength lasers. Through combined RHD simulations and NLTE calculations, we identified an optimal ionization level for generating Sn^{11+}–Sn^{14+} ions, the dominant contributors to 13.5-nm radiation. A spectral comparison in the 7–10 nm range successfully determined the charge state distribution of the experimental plasma, which showed strong consistency with the simulation predictions. The refined laser pulses achieved spatiotemporal uniformity by preventing over- and under-ionization, allowing the plasma to reach the optimal ionization level more efficiently.

Although a detailed calculation of CE was not performed in this study, recent advances in machine learning applied to NLTE calculations offer promising pathways for modeling the 13.5-nm radiation spectrum and its correlation with charge state distributions [57]. The present findings can serve as a foundation for such future efforts, providing essential guidelines for optimizing laser parameters and contributing to the development of more efficient EUV light sources.

CRediT authorship contribution statement

Jang Hyeob Sohn: Writing – review & editing, Writing – original draft, Visualization, Validation, Software, Methodology, Investigation, Formal analysis, Data curation, Conceptualization. **Hyun-Kyung Chung:** Writing – review & editing, Validation, Software, Resources. **Hyungyu Yu:** Software, Resources. **Inki Jeong:** Resources. **Sang June Hahn:** Resources. **Young-Gui Yoon:** Resources. **Hyyong Suk:** Software, Resources. **Byoung Ick Cho:** Writing – review & editing, Supervision,

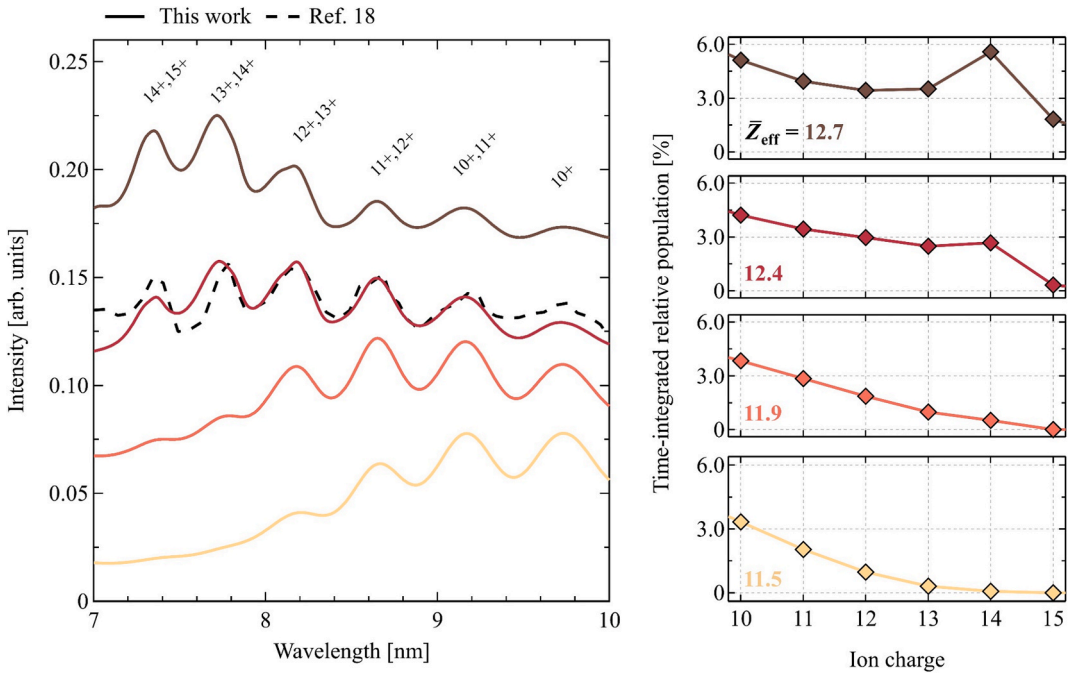

Fig. 6. Time-integrated short-wavelength spectra (left) calculated for various charge state distributions (right) of the 2-μm-driven tin plasmas, compared with the measured spectrum at the optimal intensity [18]. Each peak emission is labeled with its corresponding charge state(s). The spectra are normalized to their peak intensities at 13.5 nm and vertically offset by increments of 0.05 for clarity.

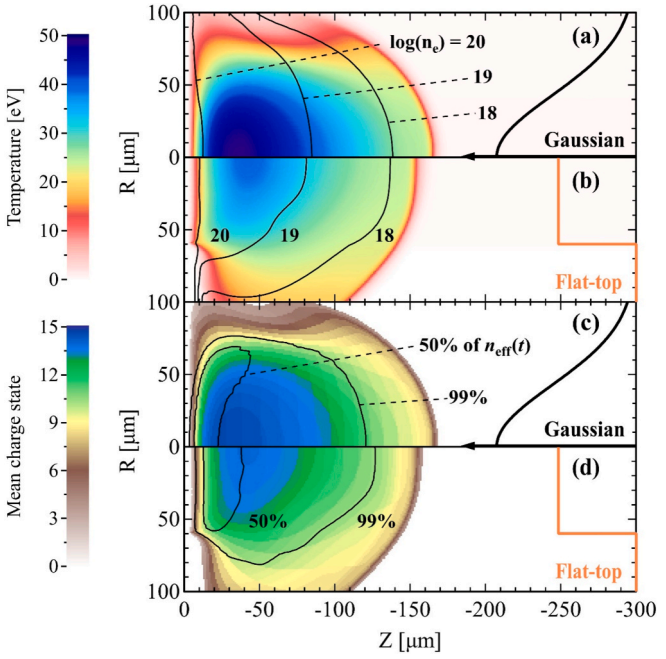

Fig. 7. Electron temperature and density distributions (at t = 4 ns) of tin plasmas produced by the 2-μm (a) Gaussian pulses and (b) flat-top pulses. (c), (d) Corresponding mean charge states and contours enclosing 50 % and 99 % of Sn^{11+}– Sn^{14+} ions. The spatial profiles of the laser pulses are indicated. Color scales differ from those in Fig. 3.

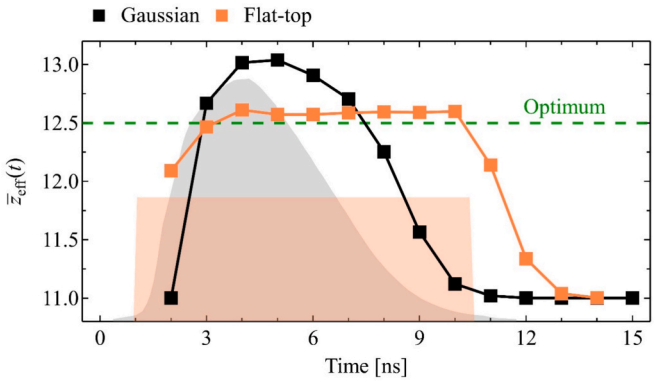

Fig. 8. Temporal evolution of the effective mean charges $\bar{z}_{eff}(t)$ for tin plasmas produced by 2-μm Gaussian and flat-top pulses. The temporal profiles of both laser pulses are shown. The green dashed line marks the optimal $\bar{z}_{eff}(t) = 12.5$.

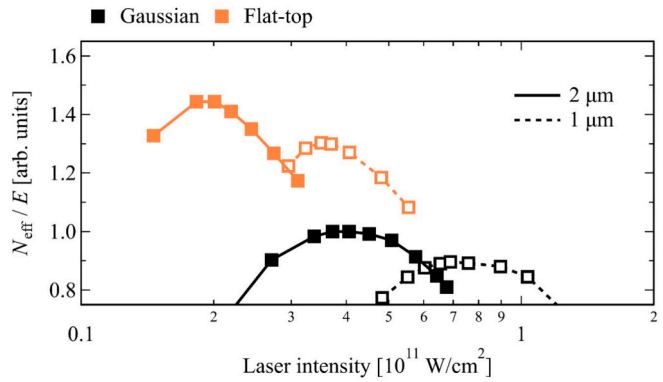

Fig. 9. Normalized ratio N_{eff}/E for the 2- and 1-μm Gaussian and flat-top pulses, plotted as a function of laser intensity.

Project administration, Funding acquisition, Conceptualization.

Declaration of competing interest

The authors declare that they have no known competing financial interests or personal relationships that could have appeared to influence

the work reported in this paper.

Acknowledgements

This work was supported by the Institute for Basic Science (IBS-R038-D1) and the National Research Foundation of Korea (Nos. RS-2022-00207260, RS-2023-00218180, RS-2025-00516264).

Data availability

Data will be made available on request.

References

[1] Nishihara K, Sunahara A, Sasaki A, Nunami M, Tanuma H, Fujioka S, et al. Plasma physics and radiation hydrodynamics in developing an extreme ultraviolet light source for lithography. Phys. Plasmas 2008;15:056708.
[2] Nowak KM, Ohta T, Suganuma T, Fujimoto J, Mizoguchi H, Sumitani A, et al. CO_2 laser drives extreme ultraviolet nano-lithography – second life of mature laser technology. Opto-Electron. Rev. 2013;21:345.
[3] Fomenkov I, Brandt D, Ershov A, Schafgans A, Tao Y, Vaschenko G, et al. Light sources for high-volume manufacturing EUV lithography: technology, performance, and power scaling. Adv. Opt. Technol. 2017;6:173.
[4] Purvis M, Fomenkov IV, Schafgans AA, Vargas M, Rich S, Tao Y, et al. Industrialization of a robust EUV source for high-volume manufacturing and power scaling beyond 250W. Proc. SPIE 2018;10583:1058327.
[5] Versolato OO. Physics of laser-driven tin plasma sources of EUV radiation for nanolithography. Plasma Sources Sci. Technol. 2019;28:083001.
[6] Versolato OO, Sheil J, Witte S, Ubachs W, Hoekstra R. Microdroplet-tin plasma sources of EUV radiation driven by solid-state-lasers (Topical Review). J. Opt. 2022;24:054014.
[7] Bajt S, Alameda JB, Barbee Jr TW, Clift WM, Folta JA, Kaufmann BB, et al. Improved reflectance and stability of Mo/Si multilayers. Opt. Eng. 2002;41:1797.
[8] Huang Q, Medvedev V, van de Kruijs R, Yakshin A, Louis E, Bijkerk F. Spectral tailoring of nanoscale EUV and soft x-ray multilayer optics. Appl. Phys. Rev. 2017;4:011104.
[9] Tamer I, Reagan BA, Galvin T, Galbraith J, Sistrunk E, Church A, et al. Demonstration of a compact, multi-joule, diode-pumped Tm:YLF laser. Opt. Lett. 2021;46:5096.
[10] Meijer RA, Stodolna AS, Eikema KSE, Witte S. High-energy Nd:YAG laser system with arbitrary sub-nanosecond pulse shaping capability. Opt. Lett. 2017;42:2758.
[11] Yin L, Wang H, Reagan BA, Baumgarten C, Lyu Z, Soufli R, et al. Using temporally synthesized laser pulses to enhance the conversion efficiency of Sn plasmas for EUV lithography. IEEE Photonics J. 2021;13:1700115.
[12] Tamer I, Reagan BA, Galvin T, Batysta F, Sistrunk E, Willard D, et al. 1 GW peak power and 100 J pulsed operation of a diode-pumped Tm:YLF laser. Opt. Express 2022;30:46336–43.
[13] Tamer I, Reagan BA, Batysta F, Kiani L, Hubka Z, Galvin T, et al. High energy operation of a diode-pumped Tm:YLF laser. Proc. SPIE 2023;12401:1240109.
[14] Tamer I, Hubka Z, Kiani L, Owens J, Church A, Batysta F, et al. Demonstration of a 1 TW peak power, joule-level ultrashort Tm:YLF laser. Opt. Lett. 2024;49:1583–6.
[15] Schupp R, Torretti F, Meijer RA, Bayraktar M, Sheil J, Scheers J, et al. Radiation transport and scaling of optical depth in Nd:YAG laser-produced microdroplet-tin plasma. Appl. Phys. Lett. 2019;115:124101.
[16] Schupp R, Torretti F, Meijer RA, Bayraktar M, Scheers J, Kurilovich D, et al. Efficient generation of extreme ultraviolet light from Nd:YAG-driven microdroplet-tin plasma. Phys. Rev. Appl 2019;12:014010.
[17] Schupp R, Behnke L, Bouza Z, Mazzotta Z, Mostafa Y, Lassise A, et al. Characterization of angularly resolved EUV emission from 2-μm-wavelength laser-driven Sn plasmas using preformed liquid disk targets. J. Phys. D Appl. Phys. 2021;54:365103.
[18] Behnke L, Schupp R, Bouza Z, Bayraktar M, Mazzotta Z, Meijer R, et al. Extreme ultraviolet light from a tin plasma driven by a 2-μm-wavelength laser. Opt. Express 2021;29:4475.
[19] Schupp R, Behnke L, Sheil J, Bouza Z, Bayraktar M, Ubachs W, et al. Characterization of 1- and 2-μm-wavelength laser-produced microdroplet-tin plasma for generating extreme-ultraviolet light. Phys. Rev. Res. 2021;3:013294.
[20] Sizyuk T, Hassanein A. Tuning laser wavelength and pulse duration to improve the conversion efficiency of EUV sources. Phys. Plasmas 2020;27:103507.
[21] Hemminga DJ, Versolato OO, Sheil J. Simulations of plasmas driven by laser wavelengths in the 1.064—10.6 μm range for their characterization as future extreme ultraviolet light sources. Phys. Plasmas 2023;30:033301.
[22] Mostafa Y, Behnke L, Engels DJ, Bouza Z, Sheil J, Ubachs W, et al. Production of 13.5 nm light with 5% conversion efficiency from 2 μm laser-driven tin microdroplet plasma. Appl. Phys. Lett. 2023;123:234101.
[23] Yuan Y, Ma YY, Wang WP, Chen SJ, Cui Y, Zi M, et al. Enhancing the conversion efficiency of extreme ultraviolet light sources using a 2 μm wavelength laser. Plasma Phys Control Fusion 2022;64:025001.
[24] Shi ZY, Yuan Y, Wang WP, Ma YY, Sun XY, Lin N, et al. Enhanced extreme ultraviolet conversion efficiency of a 2 μm laser-driven preformed tin-droplet target using short picosecond pre-pulses. Phys. Plasmas 2023;30:043107.
[25] Torretti F, Schupp R, Kurilovich D, Bayerle A, Scheers J, Ubachs W, et al. Short-wavelength out-of-band EUV emission from Sn laser-produced plasma. J. Phys. B: At. Mol. Opt. Phys. 2018;51:045005.
[26] Torretti F, Liu F, Bayraktar M, Scheers J, Bouza Z, Ubachs W, et al. Spectral characterization of an industrial EUV light source for nanolithography. J. Phys. D Appl. Phys. 2020;53:055204.
[27] Torretti F, Sheil J, Schupp R, Basko MM, Bayraktar M, Meijer RA, et al. Prominent radiative contributions from multiply-excited states in laser-produced tin plasma for nanolithography. Nat. Commun. 2020;11:2334.
[28] Sheil J, Versolato OO, Neukirch AJ, Colgan J. Multiply-excited states and their contribution to opacity in CO_2 laser-driven tin-plasma conditions. J. Phys. B: At. Mol. Opt. Phys. 2021;54:035002.
[29] Kauffman RL, Phillion DW, Spitzer RC. X-ray production ~13 nm from laser-produced plasmas for projection x-ray lithography applications. Appl. Opt. 1993;32:6897–900.
[30] Shimada Y, Nishimura H, Nakai M, Hashimoto K, Yamaura M, Tao Y, et al. Characterization of extreme ultraviolet emission from laser-produced spherical tin plasma generated with multiple laser beams. Appl. Phys. Lett. 2005;86:051501.
[31] Harilal SS, O'Shay B, Tillack MS, Tao Y, Paguio R, Nikroo A, et al. Spectral control of emissions from tin doped targets for extreme ultraviolet lithography. J. Phys. D Appl. Phys. 2006;39:484.
[32] Hayden P, Cummings A, Murphy N, O'Sullivan G, Sheridan P, White J, et al. 13.5nm extreme ultraviolet emission from tin based laser produced plasma sources. J. Appl. Phys. 2006;99:093302.
[33] Okuno T, Fujioka S, Nishimura H, Tao Y, Nagai K, Gu Q, et al. Low-density tin targets for efficient extreme ultraviolet light emission from laser-produced plasmas. Appl. Phys. Lett. 2006;88:161501.
[34] White J, Dunne P, Hayden P, O'Reilly F, O'Sullivan G. Optimizing 13.5nm laser-produced tin plasma emission as a function of laser wavelength. Appl. Phys. Lett. 2007;90:181502.
[35] George SA, Silfvast WT, Takenoshita K, Bernath RT, Koay CS, Shimkaveg G, et al. Comparative extreme ultraviolet emission measurements for lithium and tin laser plasmas. Opt. Lett. 2007;32:997–9.
[36] Fujioka S, Nishimura H, Nishihara K, Sasaki A, Sunahara A, Okuno T, et al. Opacity effect on extreme ultraviolet radiation from laser-produced tin plasmas. Phys. Rev. Lett. 2005;95:235004.
[37] Ando T, Fujioka S, Nishimura H, Ueda N, Yasuda Y, Nagai K, et al. Optimum laser pulse duration for efficient extreme ultraviolet light generation from laser-produced tin plasmas. Appl. Phys. Lett. 2006;89:151501.
[38] Tao Y, Harilal S, Tillack M, Sequoia K, O'Shay B, Najmabadi F. Effect of focal spot size on in-band 13.5 nm extreme ultraviolet emission from laser-produced Sn plasma. Opt. Lett. 2006;31:2492.
[39] Yuspeh S, Sequoia KL, Tao Y, Tillack MS, Burdt R, Najmabadi F. Optimization of the size ratio of Sn sphere and laser focal spot for an extreme ultraviolet light source. Appl. Phys. Lett. 2008;93:221503.
[40] Yuspeh S, Tao Y, Burdt R, Tillack M, Ueno Y, Najmabadi F. Dynamics of laser-produced Sn microplasma for a high-brightness extreme ultraviolet light source. Appl. Phys. Lett. 2011;98:201501.
[41] Sasaki A, Sunahara A, Furukawa H, Nishihara K, Fujioka S, Nishikawa T, et al. Modeling of radiative properties of Sn plasmas for extreme-ultraviolet source. J. Appl. Phys. 2010;107:113303.
[42] Colgan J, Kilcrease DP, Abdallah Jr J, Sherrill ME, Fontes CJ, Hakel P, et al. Atomic structure considerations for the low-temperature opacity of Sn. High Energy Density Phys. 2017;23:133137.
[43] Fryxell B, Olson K, Ricker P, Timmes FX, Zingale M, Lamb DQ, et al. FLASH: an adaptive mesh hydrodynamics code for modeling astrophysical thermonuclear flashes. Astrophys. J. Suppl. Ser. 2000;131:273.
[44] Faik S, Tauschwitz A, Iosilevskiy I. The equation of state package FEOS for high energy density matter. Comput. Phys. Commun. 2018;227:117.
[45] Chung H-K, Chen MH, Morgan WL, Ralchenko Y, Lee RW. FLYCHK:generalized population kinetics and spectral model for rapid spectroscopic analysis for all elements. High Energy Density Phys. 2005;1:3.
[46] Griem HR. Validity of local thermal equilibrium in plasma spectroscopy. Phys. Rev. 1963;131:1170.
[47] Cho MS, Matsuo K, Fujioka S, Hahn SJ, Cho BI, Chung H-K. Opacity calculation for aluminum, iron, and gold plasmas using FLYCHK code. J. Quant. Spectrosc. Radiat. Transf. 2020;257:107369.
[48] Cho MS, Sohn JH, Chung H-K, Cho BI, Hahn SJ. Analysis of the FLYCHK opacity of X-pinch wire materials. J Kor Phys Soc 2021;78:1072.
[49] Sohn JH, Cho MS, Chung H-K, Cho BI, Hahn SJ. Opacity calculations for aluminum, hydrogen, and gold using FLYCHK with improved free-free opacity formalism. Curr. Appl Phys. 2023;51:53.
[50] Tanabe M, Nishimura H, Ohnishi N, Fournier KB, Fujioka S, Iwamae A, et al. Characterization of heat-wave propagation through laser-driven Ti-doped underdense plasma. High Energy Density Phys. 2010;6:89.
[51] Hoarty DJ, Allan P, James SF, Brown CRD, Hobbs LMR, Hill MP, et al. Observations of the effect of ionization-potential depression in hot dense plasma. Phys. Rev. Lett. 2013;110:265003.
[52] Kaur C, Chaurasia S, Poswal AK, Munda DS, Rossall AK, Deo MN, et al. K-shell X-ray spectroscopy of laser produced aluminum plasma. J. Quant. Spectrosc. Radiat. Transfer 2017;187:20.
[53] Humphries OS, Allan P, Brown CRD, Hobbs LMR, James SF, Ramsay MG, et al. Time evolution of transient plasma states from nanowire arrays irradiated at relativistic intensities. Commun. Phys. 2020;3:170.
[54] Chen MH, Laiman E, Casemann B, Aoyagi M, Mark H. Relativistic L-shell Auger and Coster–Kronig rates and fluorescence yields. Phys. Rev. A 1979;19:2253.

[55] Cho BI, Engelhorn K, Vinko SM, Chung H-K, Ciricosta O, Rackstraw DS, et al. Resonant Kα spectroscopy of solid-density aluminum plasmas. Phys. Rev. Lett. 2012;109:245003.
[56] Su MG, Min Q, Cao SQ, Sun DX, Hayden P, O'Sullivan G, et al. Evolution analysis of EUV radiation from laser-produced tin plasmas based on a radiation hydrodynamics model. Sci. Rep. 2017;7:45212.
[57] Cho MS, Grabowski PE, Thopalli K, Jayram TS, Barrow MJ, Thiagarajan JJ, et al. Physics-informed transformation toward improving the machine-learned NLTE models of ICF simulations. Phys. Rev. Res. 2025;7:023150.